Effect of welding parameters on the solidification microstructure of autogenous TIG welds in an Al–Cu–Mg–Mn alloy

A.F. Norman *, V. Drazhner, P.B. Prangnell

Manchester Materials Science Centre, University of Manchester/UMIST, Grosvenor Street, Manchester, M1 7HS, UK

Abstract

The weld metal microstructures of autogenous TIG welds have been investigated for a range of welding conditions using an Al–Cu–Mg–Mn alloy. It was found that a combination of high welding speeds and low power densities provide the thermal conditions required for the nucleation and growth of equiaxed grains in the weld pool, providing heterogeneous nucleation sites are available. The most likely origin of the nucleants is from a combination of dendrite fragments and TiB_2 particles that survive in the weld pool. The finest microstructure was observed in the centre of the weld and is attributed to the higher cooling rates which operate along the weld centreline. Composition profiles across the dendrite side arms were measured in the TEM and were found to follow a Scheil type segregation behaviour where there is negligible back diffusion in the solid. The measured core concentration of the dendrite side arms was found to rise with increasing welding speed and was attributed to the formation of significant undercoolings ahead of the primary dendrite tip, which enriched the liquid surrounding the dendrite side arms. © 1999 Elsevier Science S.A. All rights reserved.

Keywords: TIG welding; Al–Cu–Mg–Mn alloys; Grain structures; Microsegregation

1. Introduction

Heat treatable AA2000 series aluminium alloys are among the most widely used materials for structural applications where high strength to density ratios are important. In many applications, the dominant joining process is through the use of mechanical fasteners (rivets). Typically a large numbers of fasteners are used, which makes assembling primary structures an extremely tedious and time consuming process. Additional problems arise because a wide flange is required and the section thickness of each component is usually increased around the joint producing a further weight penalty. Riveted joints are also relatively inefficient, in terms of strength, and act as sites for rapid fatigue crack initiation [1].

If welding could be utilised without significantly increasing the section thickness of the joint, then a con-

siderable advantage in the manufacturing process would result, both in terms of weight savings and a reduction in the fabrication time. At present the weldability of the most widely used AA2000 series aluminium alloys is known to be poor [1,3]. This is in contrast to alloys used in the former Soviet Union, where a number of weldable aluminium compositions have been developed, and are used in both aerospace and automotive applications [4–6]. Furthermore there is also some evidence to suggest that welded joints perform better in fatigue than riveted joints [2].

The fusion welding of high strength AA2000 series aluminium alloys was given some attention in the early 1960s [7,8]. Despite the fact that at the time, welding technology was more primitive, several problems associated with the welding of AA2000 series aluminium alloys were identified. These included the poor strength and ductility of the weld metal, solidification cracking, and grain boundary melting in the heat affected zone (HAZ) [7]. Recently the macroscopic grain structures of Al alloy TIG welds have been investigated by a number

* Corresponding author. Tel.: +44 161 2003588; fax: +44 161 2003586; e-mail: andy.norman@umist.ac.uk

Table 1
Welding conditions for the samples under investigation

Sample No.	Welding speed (mm s^{-1})	Welding current (A)	Power[a] (W)	Power density[b] (J mm^{-3})
1	7	100	630	14.8
2	13	130	819	12.3
3	19	160	1008	10.4
4	25	190	1197	8.3

[a] Calculated from $Q = \eta IV$, where Q is the total heat input, V is the welding voltage and, η is taken to be 0.70 [10].
[b] The volume of weld per second is estimated from width × thickness × welding speed.

of researchers [9–12]. It is widely accepted that equiaxed dendritic grains tend to form in the centre of the weld, at high welding speeds, whereas columnar structures (otherwise known as axial or stray grains) usually form at low welding speeds.

Only a limited number of researchers have focused on the microsegregation behaviour in Al alloy TIG welds [13,14]. However, understanding the redistribution of solute during solidification is particularly important in heat treatable alloys as the weld metal strength will depend on the solute supersaturation, which determines the subsequent ageing response and yield strength. In order to develop models capable of predicting the weld metal properties, it is equally important to be able to predict the grain structure and dendrite arm spacing and volume fraction of eutectic, which will dominate the toughness and ductility. A number of workers have demonstrated that a relatively simple approach, based on estimating the cooling rate can be used to reliably predict dendrite arm spacings in model aluminium alloys [15], but this has not yet been attempted with more complex alloys of near commercial composition. Furthermore, there is little experimental data available in the literature comparing measurements of solute profiles across dendrites to models of solute redistribution. Conflicting results exist between measured solute profiles; some workers suggesting a Scheil behaviour [16], where there is effectively no diffusion in the solid phase, and other profiles based on the model of Brody and Fleming [17], where there is limited back diffusion in the solid.

In this paper, results are presented on the commercial aluminium alloy AA2024 which has been autogenously TIG welded using a range of processing conditions. Although in practice it is unlikely that structures would be welded without the use of filler materials, the addition of a filler material makes the prediction of the microstructure in the weld more difficult. The welds were characterised using optical metallography to reveal the different grain structures, produced with different welding conditions. The sub-grain structures were studied using a combination of techniques. Scanning electron microscopy (SEM) was used to measure the dendrite secondary arm spacing at different positions in each weld, whereas transmission electron microscopy (TEM), EDX analysis, and X-ray diffraction were used to measure the effect of the welding speed on the segregation behaviour of the major alloying elements, and the phases which formed on solidification. The results are compared to existing models to see if it is possible to predict the main features of the weld microstructure in multi-component alloys, as a function of the welding parameters, without resorting to thermodynamic calculations which require extensive computing power.

2. Experimental

The commercial aluminium alloy AA2024 (Al–4.4 wt% Cu–1.5 wt% Mg–0.8 wt% Mn, and Fe and Si impurities) was TIG welded autogenously, using the range of conditions given in Table 1. The sheet thickness was 1.6 mm and a simple butt geometry was used for each experiment. The experiments were designed such that, as the welding speed was increased, the welding current was also increased to just maintain full penetration of the weld. The data in Table 1 shows that, with increasing welding speed, the overall power density required to maintain full penetration decreases. After welding, the samples were sectioned and mounted either along the direction of the weld in plan view or sectioned through the weld (transverse view). Each sample was examined using conventional optical microscopy. Samples for SEM examination were prepared by polishing to 1 μm finish and electropolishing in a solution of 10 vol% nitric acid in methanol at 20 V, and −30°C.

Thin foils for TEM observation were prepared from the welds by spark eroding 3 mm discs from different positions in the weld sample. The discs were ground to a thickness of ~100 μm and jet-polished using a solution of 30 vol% nitric acid in methanol at −30°C and 12 V. The foils were examined in a Philips CM 200 analytical TEM operated at 200 kV. Quantitative EDX analysis was performed by traversing across several dendrite side arms for each welding speed. The core concentration of the side arms was determined as a function of welding speed (approximately 15 arms were measured for each speed). Because of the strong likeli-

hood of dendrites not being sectioned through their centre in a random section, only the widest dendrites were analysed and the lowest core concentration measured was used as the most representative value. All EDX data was ZAF corrected and compositions were measured across dendrite side arms in positions where the eutectic phase had been polished out of the foil, thus eliminating the possibility of unrepresentative measurements near the dendrite boundary.

3. Macroscopic grain structures

3.1. Formation of fusion zone microstructures

In autogenous TIG welding, the macroscopic grain structure is controlled by a combination of the thermal conditions that prevail at the solid–liquid interface and the crystal growth rate which is directly related to the welding speed [14]. The thermal conditions are determined by the heat input and the weld speed for a given sheet thickness. Furthermore, the conditions vary considerably depending on the position at the solid–liquid interface along the trailing edge of the weld pool. For thin sheet Al alloys, the high thermal diffusivity of aluminium favours the formation of an elliptical weld pool shape, even at relatively high heat inputs and welding speeds [18].

The different types of grain structures observed, as a function of the welding conditions, are shown in Fig. 1 and are summarised in Fig. 2. For the lowest welding speed considered (7 mm s^{-1}) a few extremely long columnar-dendritic grains were observed (often termed 'axial' [11]), which grew along the centre of the weld in the direction of the motion of the heat source (Fig. 2(a)). The overall width of this weld was ~4 mm and the columnar-dendritic region was around 1 mm wide. The axial grain structure shown in Fig. 1(a) has been reported for other TIG welded Al alloys, such as AA3003 (Al–Fe–Mn) and AA5454 (Al–Mg) [9] which were also produced at low welding speeds and heat inputs. On either side of the central axial grains, columnar-dendritic grains were found, which solidified on the base metal (epitaxial nucleation) and grew towards the central axial region (Fig. 1(b)). The epitaxially grown dendrites curve towards the heat source, so that the maximum thermal gradients present at the solid–liquid interface, are maintained as growth proceeds. For the sample with the lowest speed (7 mm s^{-1}), near the end of the weld, the central region became slightly wider and the density of grains increased, producing a more 'stray-like' grain structure (Fig. 1(c)). This effect was probably due to the sheet metal increasing in temperature as the weld proceeded which reduced the thermal gradients at the solid–liquid interface. The weld with the next highest speed (13 mm s^{-1}) had a stray grain

structure along the central region of the weld, throughout the entire weld length. It has been reported by Ganaha et al. [9] that stray grain structures usually form at intermediate welding speeds and heat inputs, and are characterised by the continual appearance of new anisotropic grains aligned along the central region of the weld, in the welding direction. As the nucleation rate at the interface is very low, many of the grains grow a considerable distance in the direction of the heat source, and therefore appear elongated in morphology.

At all higher welding speeds, the central region of the weld consisted of an equiaxed-dendritic structure with an average grain size of ~250 μm (Fig. 1(d)). The remaining weld microstructure still consisted of epitaxial columnar grains growing in from the weld edge. The equiaxed region covered almost a third of the width of the weld produced at 19 mm s^{-1}, which increased to almost half the weld width at 25 mm s^{-1}. These welds were also examined in the transverse direction and show that for the two highest welding speeds, a region of equiaxed grains formed throughout the thickness of the weld (Fig. 1(e) and (f)).

3.2. Columnar to equiaxed transition (CET)

In this work, a transition series from axial, to stray, to equiaxed grains, was observed as the welding speed was increased (shown in Fig. 2(d)). The same type of transition has previously been reported for a range of other TIG welded Al alloys; namely AA6061 [10], AA1100, AA5052, and AA7004 [9], and as can be seen in Fig. 2(d), the columnar to equiaxed transition occurs at roughly the same welding speed/heat input combinations, despite the difference in alloy compositions. Hunt [19] has analysed the conditions necessary for the growth of equiaxed grains ahead of a columnar interface during directional solidification. Hunt's analysis, which assumes that a 50% equiaxed volume fraction is sufficient to block columnar growth, results in the following expression for predicting the columnar-to-equiaxed (CET) transition:

$$G_L < 0.061 N_0^{1/3}\left[1 - \frac{(\Delta T_N)^3}{(\Delta T_C)^3}\right]\Delta T_C \qquad (1)$$

where G_L is the maximum thermal gradient, N_0 is the density of heterogeneous nucleants, ΔT_N is the critical undercooling for heterogeneous nucleation, and ΔT_C is the growth undercooling at the columnar front. Although these quantities cannot be easily established, Eq. (1) suggests that the formation of equiaxed grains in the centre of the weld can be expected providing that; (i) there is a supply of nucleation sites from which new grains may develop, and (ii) thermal conditions are present which favour the nucleation and growth of new grains. It should be noted that the transition from columnar to equiaxed grains also requires a sufficiently

Fig. 1. Examples of the different grain structures found in 2024 autogenous TIG welds for the different welding speeds. (a) Axial, 7 mm s^{-1} (plan); (b) epitaxial, 7 mm s^{-1} (plan); (c) stray, 13 mm s^{-1} (plan); (d) equiaxed, 25 mm s^{-1} (plan); (e) equiaxed, 25 mm s^{-1} (transverse); and (f) equiaxed, 25 mm s^{-1} (transverse).

high nucleation rate relative to the growth rate. The two conditions noted above are explained in more detail below.

3.2.1. Supply of nucleants

In the welding of Al alloys, the formation of new grains can originate from two sources; the growth of pre-existing nuclei created by dendrite fragmentation, or by grain detachment, and heterogeneous nucleation at second phase particles present in the melt, or impurities in the weld pool [14]. It is well known that the grain structure of cast ingots is controlled through the deliberate addition of inoculants [20]. During welding it is possible for some of the inoculants to survive in the weld pool and act as nucleants for new grains. The alloy examined in this work also contains a small addition of TiB$_2$ particles, which are used to control the grain structure during DC casting, and therefore it is

possible for some of these particles to act as nucleants in the weld pool. Recently there has been some direct evidence of Ti rich particles acting as nucleants for grains in TIG welds of Al alloys AA6061 [10] and AA7004 [9]. It is also interesting to note that for the Al alloy AA5083, which contains a significant amount of Ti (0.024 wt%), a region of equiaxed grains was observed at both low and high welding speeds [9]. Also, when the alloy AA2024 is welded with the filler AA2319 (which contains grain refining additions of Ti and Zr), the welding speed at which the columnar to equiaxed tran-
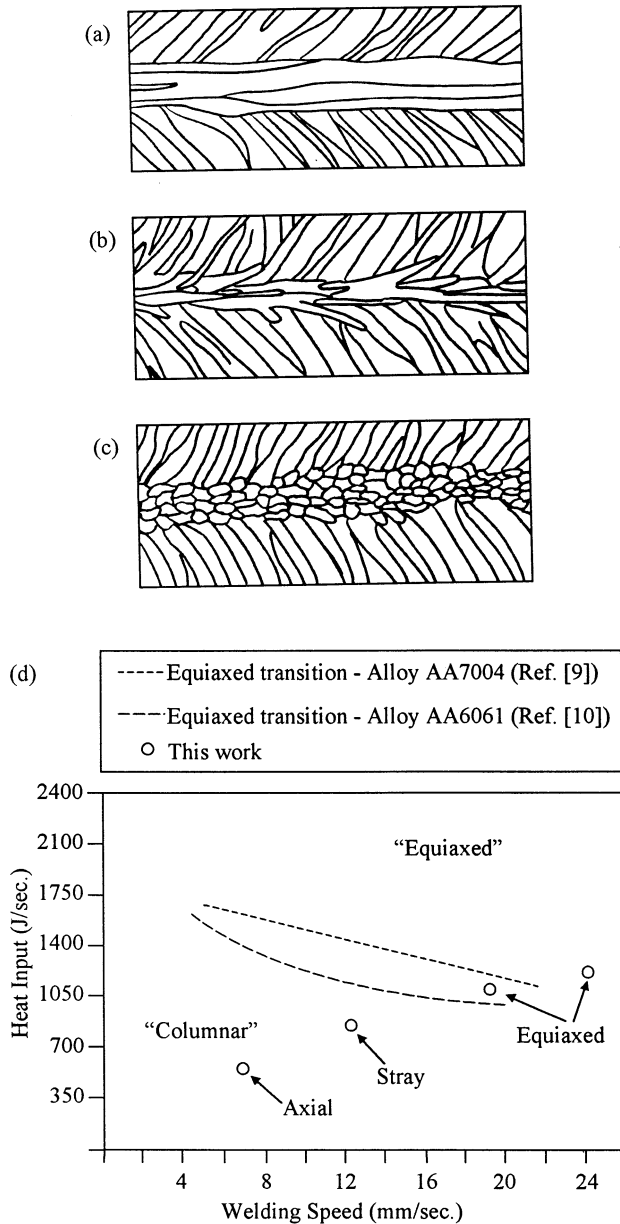

Fig. 2. Schematic diagrams illustrating the different types of grain structures found in Al TIG welds. (a) Axial, (b) Stray, (c) equiaxed, and (d) a plot of heat input versus welding speed for the different welds produced in this work.

sition occurs is reduced from 15 to around 6 mm s^{-1} [24].

3.2.2. Thermal considerations

For the welds studied in this work, an increase in the welding speed was accompanied by an increase in the welding current so that full weld penetration was maintained. However, the power density (see Table 1) decreased as the welding speed was increased. This combination of conditions can cause a decreasing, or nearly constant thermal gradient in the liquid, whilst promoting an increase in the crystal growth velocity. If the thermal gradient decreases, with increasing weld speed, this could result in significant undercoolings ahead of the solid–liquid interface, due to a combination of solutal and dendrite tip curvature effects (see also Section 5) [21].

In many of the previous studies on the grain structure of Al TIG welds, the temperature gradient along the weld centreline has not been measured experimentally, but has been calculated using the following equation, which is derived from the Rosenthal thin plate solution [22,23]:

$$G_L = 2\pi\alpha\rho C \left(\frac{t}{Q}\right)^2 v(T_m - T_0)^3 \qquad (2)$$

In Eq. (2), α is the thermal conductivity, ρ is the density, Q is the total heat input, C is the specific heat, t is the plate thickness, T_m is the freezing temperature and T_0 is the ambient temperature.

The calculated values of G_L for the different welding speeds are given in Table 2. The values range from 81 K mm^{-1}, at a speed of 13 mm s^{-1} to 73 K mm^{-1}, at the highest welding speed of 25 mm s^{-1}, and are thus predicted to be nearly constant in the present experiment. According to observations made by Kou and Le [10], of experimentally determined thermal gradients from thermocouples, the measured results agreed well with the calculated values at low welding speeds and heat inputs, but were increasingly inaccurate at higher speeds and power densities. This difference was attributed to the basic assumption that the heat source in the calculation is treated as a line source and neglects the presence of the weld pool, or heat flow by convection. Therefore the calculated values quoted in this work should be taken as an upper bound because it is likely that, due to convection in the weld pool, the real values would be somewhat lower resulting in a significantly decreasing thermal gradient with increasing speed (as the observed transitions in grain structure might suggest).

In this work, both the welding current and the welding speed were increased at the same time. If the effect of this was to keep the thermal gradient along the weld centreline constant, as predicted by Eq. (2), the ratio G_L/R at the weld centreline will still decrease with increasing welding speed because R increases (see Table

Table 2
Summary of calculations involving G_L and R at the weld centreline

Sample No.	Welding speed (mm s^{-1})	G_L^a (°C mm^{-1})	G_L/R	$G_L R$ (°C s^{-1})	Calculated[b] λ_2 (µm)	Measured λ_2 (µm)
1	7	74.2	10.0	519	6.2	5.8
2	13	81.5	6.0	1059	4.9	4.9
3	19	78.7	4.1	1495	4.4	3.9
4	25	73.4	2.9	1835	4.1	3.5

[a] Calculated from Eq. (2).
[b] Calculated from Eq. (4).

2) and the undercooling achieved in the liquid, ahead of the advancing solid–liquid interface will be mainly a function of the growth velocity, which for columnar grain structures, is directly related to the welding speed. At low welding speeds this suggests that even if heterogeneous nucleation sites are present in the weld pool, the thermal conditions do not favour the formation of stable nuclei, and that any grain fragments would remelt, i.e. an axial grain structure would be expected. As the welding speed is increased, the growth velocity of the solidification front will also increase producing a higher degree of undercooling, thus producing the observed transition from axial to stray grain structures. At the highest welding speed, the undercooling will be at its greatest and can give rise to a significant nucleation rate resulting in an equiaxed structure.

4. Grain sub-structures

4.1. Introduction

The observations made in Section 3 focused on the type of grain structure that formed with different welding conditions. Of equal importance is the effect of welding parameters on the grain sub-structure that forms during welding. The results in Section 3 clearly demonstrate that for the welding conditions considered in this work, the alloy always produces a weld which contains a dendritic sub-structure (irrespective of whether the grain structure is columnar or equiaxed). Fig. 3(a) and (b) show examples of a dendritic sub-structure taken at the weld centreline for two different speeds. In both optical micrographs, a dendritic growth pattern can clearly be seen (light coloured) with a dark structure present in the interdendritic regions. At the aluminium rich corner of the ternary Al–Cu–Mg system, the phase diagram is dominated by the ternary eutectic reaction between $L \rightarrow \alpha\text{-Al} + \theta(\text{Al}_2\text{Cu}) + S(\text{Al}_2\text{CuMg})$ which is reported to occur at 503°C with a composition of 26.8 wt% Cu and 6.2 wt% Mg [25]. X-ray diffraction analysis confirmed that the dendritic matrix was α-Al and the interdendritic region was a mixture of three phases, namely α-Al, $\theta(\text{Al}_2\text{Cu})$, and $S(\text{Al}_2\text{CuMg})$, i.e. the ternary eutectic. In Fig. 3(c), a

TEM image is shown of the typical eutectic growth morphology for the welding speed of 7 mm s^{-1}.

4.2. Dendrite secondary arm spacing measurements

In the solidification of cast structures, there exists a well established link between the scale of the dendritic sub-structure and the conditions under which solidification takes place. Various studies have shown that the dendrite arm spacing, measured after processing, depends directly on a combination of the thermal gradient (G_L) and growth rate (R) [14]. The dependence of the primary (λ_1) and secondary (λ_2) arm spacings, on G_L and R take the following form:

$$\lambda_1 = a_1 (G_L^2 R)^{-n} \tag{3}$$

$$\lambda_2 = a_2 (G_L R)^{-n} \tag{4}$$

where a_1 and a_2 are coefficients, whose values depend on the alloy system, and n is an exponent whose value lies between 1/4 and 1/2. The primary spacing cannot be directly related to the cooling rate ($\epsilon = G_L R$) since its dependence on G_L and R have different exponents. However, the secondary arm spacing depends on the product of $G_L R$ and can therefore be related directly to the cooling rate.

The values of $a_2 = 50$ µm [K s^{-1}]^n and $n = 1/3$ have been estimated for binary Al–4 wt% Cu alloys within the range of cooling rates considered in this work ($1–10^5$ K s^{-1} [15]). Using these constants, the secondary arm spacing along the weld centreline has been estimated from the data given in Table 2 for G_L and R (assuming R is equal to the welding speed, this might not be the case for equiaxed microstructures as the growth direction does not necessarily correspond to the weld traverse direction). This data is plotted in Fig. 4 together with secondary arm spacings measured along the weld centreline for the different welding speeds. Fig. 4 shows that as the welding speed is increased, both the measured and calculated secondary arm spacing decreases, and that there is good agreement between the measured and calculated values, over the complete range of welding conditions, although the calculated values give consistently large spacings when compared to the measured values. There are two reasons why the
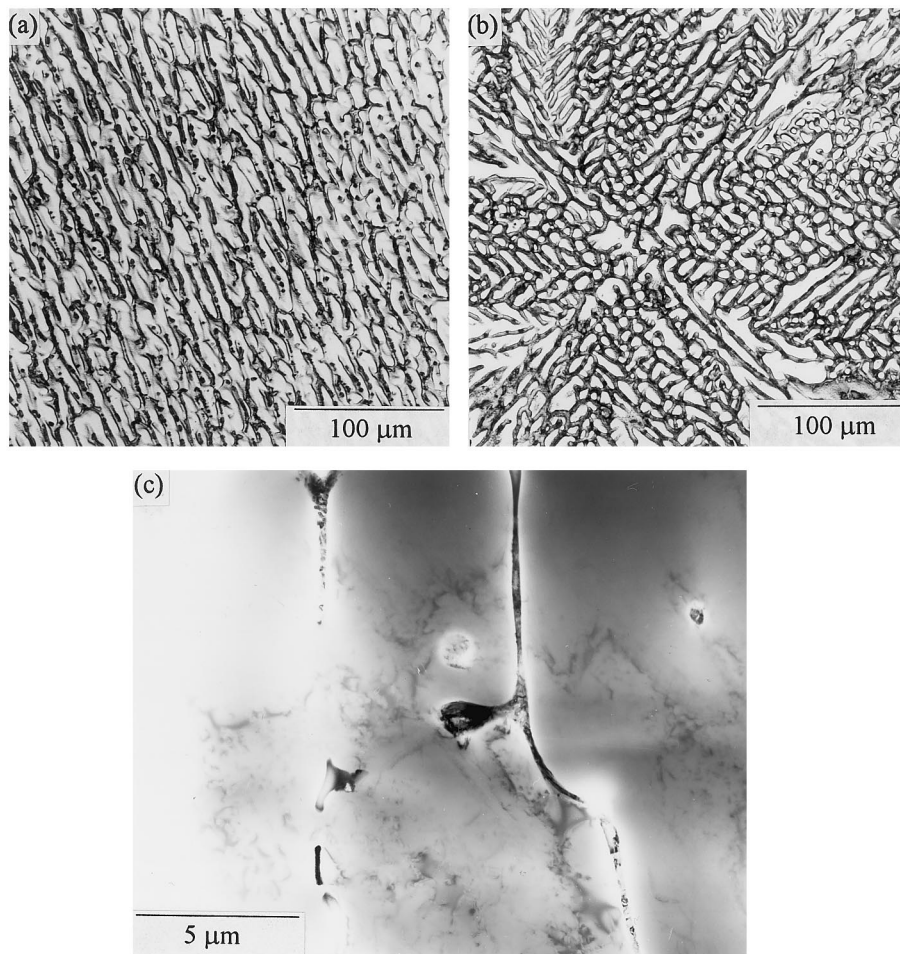
Fig. 3. (a) and (b) Optical micrographs showing the dendritic (light) and interdendritic (dark) regions along the weld centreline for the speeds of 7 and 25 mm s^{-1} respectively. (c) TEM micrograph showing the typical growth morphology of the ternary eutectic in the interdendritic regions.

calculated and measured spacings might differ. Firstly, in Section 3 we suggested that the thermal gradients calculated in Eq. (2) were to be considered as an upper estimate. If the actual values of the thermal gradient were somewhat lower (due to convection in the weld pool), then the estimated cooling rates along the weld centreline would be lower and the calculated arm spacings would be even coarser. Secondly, it is clear that a better fit between the measured and calculated spacings could be achieved by adjusting the values of the constants in Eq. (2). However, these constants have yet to be established for the commercial Al alloy 2024.

According to Eq. (4), G_L and R have the same exponent and are therefore equally important in determining the scale of the dendritic sub-structure. However, the calculated thermal gradients along the weld centreline are almost constant for the different welding speeds, so it is largely the increase in the welding speed which gives rise to the increase in cooling rate and reduction in the secondary arm spacing. Fig. 5 shows a comparison between the scale of the sub-structure along the weld centreline for the highest welding speed

and a region near the fusion boundary. The microstructures clearly show that near the fusion boundary, the sub-structure is at its coarsest, which suggests that the cooling rate at the fusion boundary is much lower than that observed in the centre of the weld. This occurs because although the thermal gradients are higher at the fusion boundary, the growth rate will be at its minimum and the overall effect will be to produce a low cooling rate compared to that observed along the weld centreline.

5. Microsegregation behaviour

5.1. Composition profiles

TEM was used to study the segregation behaviour of the alloying elements Cu and Mn within the dendrite side arms. Microanalyses were performed at different positions across dendrite side arms for the different welding speeds, and the measured variation in Cu and Mn solute contents, from the centre of a dendrite side
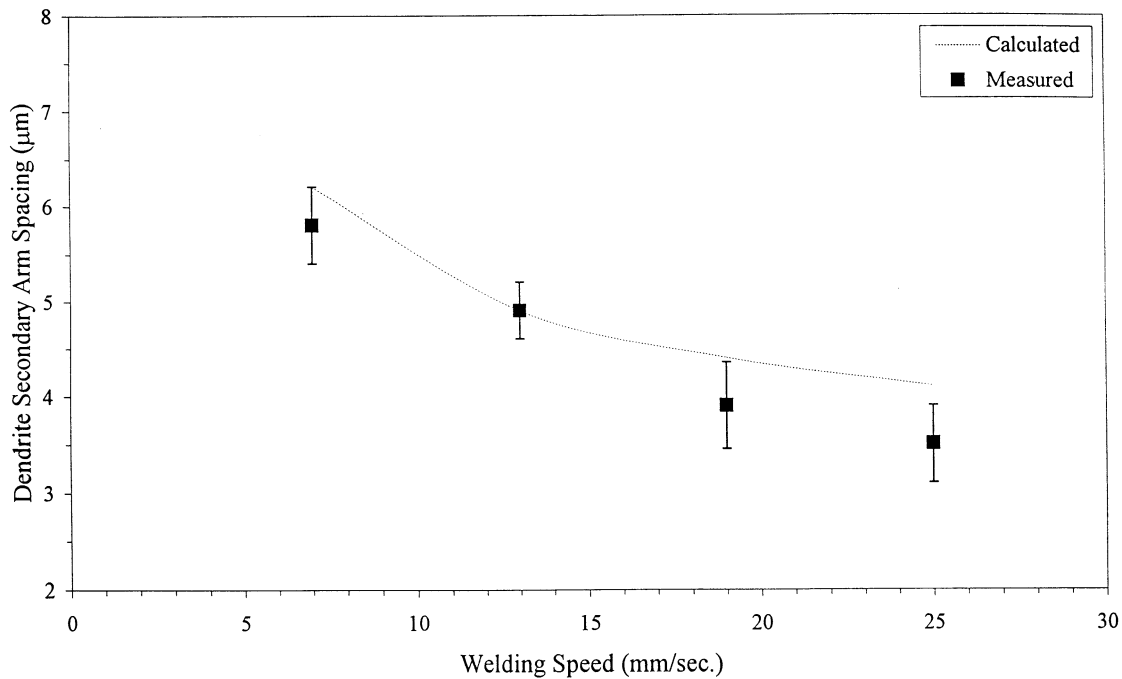
Fig. 4. Plot of measured and calculated dendrite secondary arm spacing (along the weld centreline) as a function of welding speed.

arm towards the interdendritic region. For each welding speed, five scans were made and the average values are shown in Fig. 6(a) and (b) respectively. The data in Fig. 6 was obtained from regions where the intermetallic eutectic phase had polished out of the sample on preparing the specimen, so that the results near the interdendritic region would not be affected by their presence. Mg could not be reliably analysed due to the overlap with the Al K_α peak. The spatial resolution of the measurements was ~0.2 μm which is substantially less than the dendrite arm spacings of between 4 and 5.5 μm for the welding speeds considered. Fig. 6(a) shows that, as expected, the lowest Cu concentration occurs in the core of the dendrite side arm with the Cu content increasing towards the interdendritic boundary. The profile in Fig. 6(b) also demonstrates that for Mn, the lowest concentration also occurs in the centre of the side arm, although it should be noted that the Mn content in this alloy is a lot lower than Cu.

The results clearly suggest that the segregation behaviour is more similar to the scenario envisaged by Scheil [16], where there is negligible back diffusion in the solid, than that expected by the Brody and Flemings model [17]. The Scheil equation for solute partitioning [16] is given by:

$$C_s^* = C_0 k (1 - f_s)^{k-1} \tag{5}$$

where C_s^* is the solid composition, C_0 is the initial alloy composition, f_s is the fraction of solid and k is the partition coefficient. While the Scheil equation cannot be applied directly to multi-component alloys (for non-binary systems, an iterative approach should be

adopted where the tie-lines are re-calculated at temperature increments using a thermodynamic database [26]), in a system where one alloy component dominates, such as Cu does in this case, it can be used as a rough approximation. The Scheil equation is based on the basic assumptions that the liquid is of uniform composition, local equilibrium is maintained at the solid–liquid interface (k is constant), and that there is negligible solid-state diffusion.

Whether or not there is a significant contribution of solid state diffusion to the solute redistribution process can be estimated from the parameter, η [17]:

$$\eta = \frac{D_s t_f}{\lambda_2^2} \tag{6}$$

where D_s is the solid diffusivity of the solute and t_f is the local time of freezing. For the welds produced in this work, the values of t_f are in the range 0.05–0.2 s which produces an α parameter in the range $2.4 \times 10^{-3} - 6 \times 10^{-4}$. As it can be shown that solid state diffusion during freezing only begins to become an important factor in the solute redistribution process for values of $\eta > 0.1$ [17], the freezing conditions in the weld should be similar to those predicted by the Scheil equation.

5.2. Variation of core concentration with welding speed

As the solute profiles were found to be affected by the processing conditions, the effect of welding speed on the core composition of the dendrite arm was investigated in more detail by analysing the centre of ap-
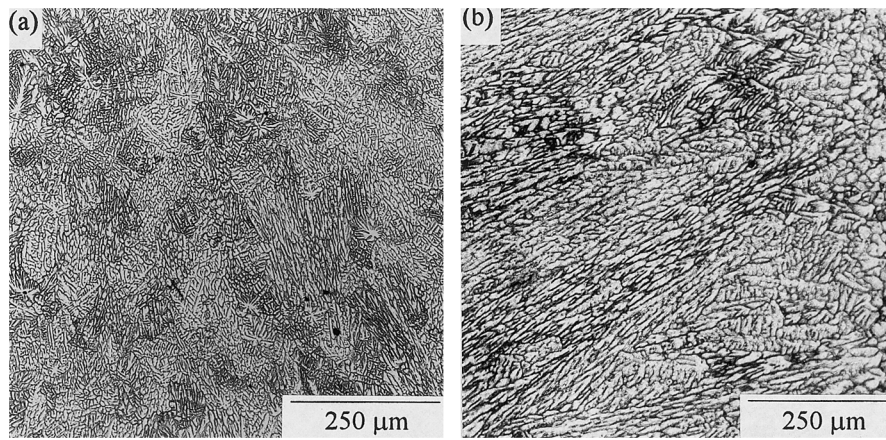
Fig. 5. Optical micrographs showing the difference in microstructural scale between (a) the weld centreline, and (b) near the fusion boundary for a welding speed of 25 mm s^{-1}.

proximately 15 side arms for each welding speed. Because of the difficulties associated with the random sectioning of dendrite side arms during the production of TEM foils, it is possible that many of the measured concentrations correspond to the composition some distance away from the centre. To reduce this risk, the widest side arms were analysed and the minimum measured concentration from 15 arms was used for each welding speed. This data is plotted in Fig. 6(c) and used in the subsequent discussion. Despite the difficulties mentioned above, the results in Fig. 6(c) clearly show that as the welding speed is increased, the dendrite core concentration of both Cu and Mn also increases, but this effect is more noticeable for Cu. Even higher core concentrations have been observed for the laser welding of AA2024 where much greater welding speeds were used [27].

To try and explain this variation in the core composition with welding speed, the arguments will be confined to analysing the behaviour of Cu, the major alloying element in 2024, as this element produced the most reliable data. Although this is a multicomponent alloy, the behaviour is compared to that of the binary Al–Cu phase diagram for simplicity, and the effect of the other alloying elements on the microsegregation behaviour of Cu in Al are neglected. As under the welding conditions used, the solid state diffusion of Cu in Al appears to be negligible (see above), it is assumed that the core concentration in the dendrite side arm corresponds to the dendrite side arm tip concentration during growth.

Under true equilibrium solidification conditions, the composition of the first solid to form will be given by $C_0 k$, where C_0 is the initial alloy concentration (equal to 4.46 wt% Cu for a binary Al–Cu alloy of the same Cu composition as AA2024) and k is the equilibrium partition coefficient (for binary Al–Cu alloys, $k = 0.17$). Using these values, the equilibrium core concentration ($C_0 k$) should be 0.76 wt% Cu, which is much lower

than that measured in any of the weld samples. Furthermore, the results shown in Fig. 6(c) demonstrate that the core concentration varies from $\sim 2C_0 k$ for the lowest welding speed to $\sim 3C_0 k$ for the highest speed considered. Similar observations have been made by Brookes and Baskes [13] who studied GTA binary Al–Cu welds containing between 1 and 2 wt% Cu. They also observed core concentrations greater than equilibrium (around $2C_0 k$–$3C_0 k$) which is in good agreement with the core concentration enrichment measured in this work.

To try and explain why the core concentration in the side arms increase with increasing welding speed, it is necessary to consider how the growth of the dendrite side arms are related to the growth of the dendrite primary tip. A schematic solute profile through the liquid in the mushy zone for dendrite growth is shown in Fig. 7. In this figure, the composition in the bulk of the liquid is given by C_0. It is possible that for the range of welding speeds considered in this work, significant undercoolings can be achieved at the primary dendrite tip which will enrich the liquid at the tip, to a composition C_t. Microstructural observations have shown that a significant volume fraction of eutectic phases are formed in the mushy zone at the end of solidification, i.e. at the root of the dendrites in the interdendritic regions (see Fig. 3(c)). Therefore, the solute profile in the liquid will change as it moves through the mushy zone, from C_t to C_E, the eutectic composition, as shown in Fig. 7. In the region where the secondary arms form, the local liquid composition will thus be enriched with solute to a level somewhere between C_t and C_E, i.e. the core concentration of the dendrite side arm will be given by $k(C_t + \Delta C)$, where ΔC depends on the relative distance back from the tip where the secondary arms form (thought to be of the order of two to three secondary arm spacings [17]).
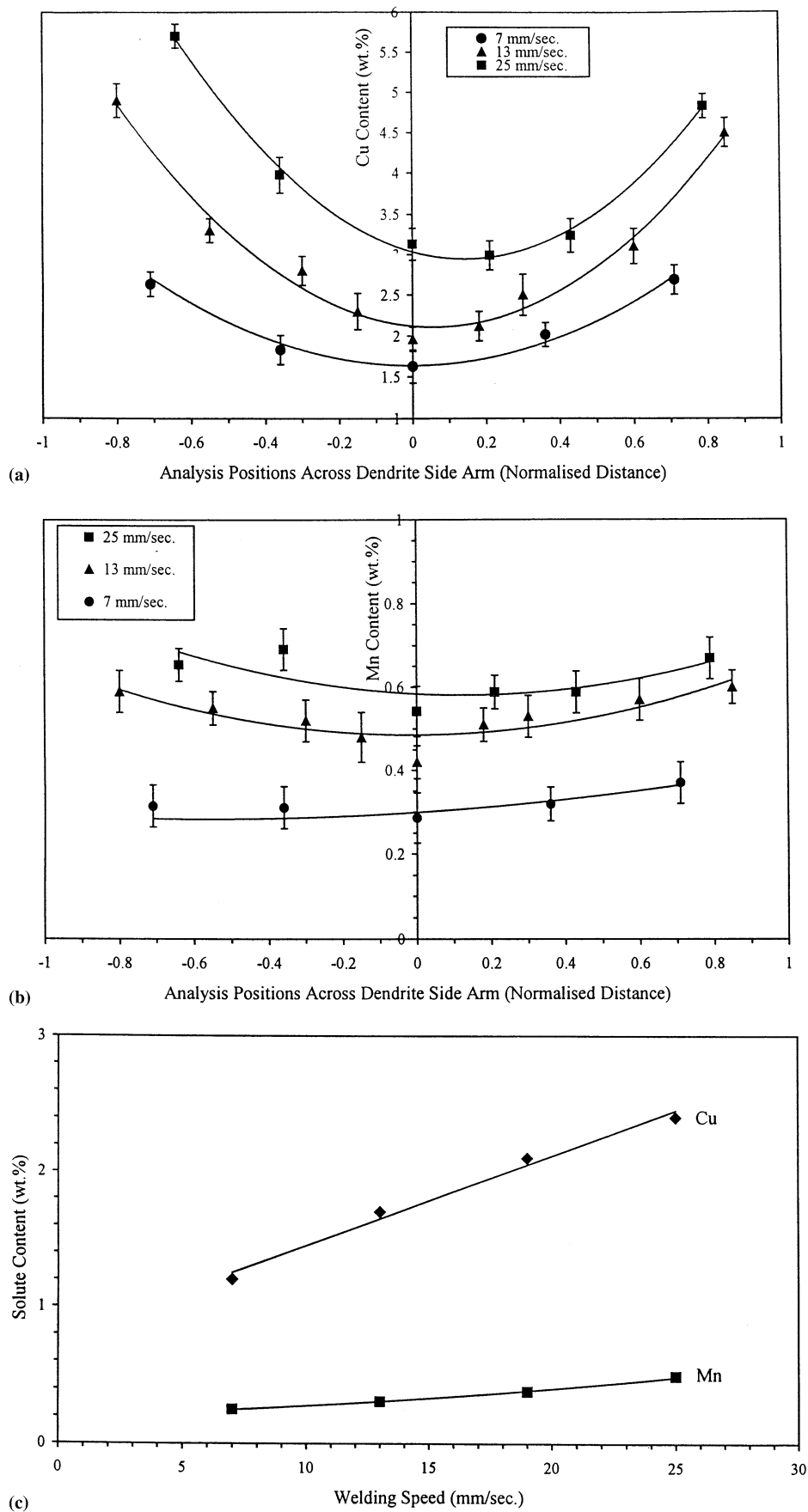
(a)

(b)

(c)

Fig. 6. EDX analyses across dendrite side arms, for (a) Cu and (b) Mn, and (c) a plot of the measured minimum core concentration for dendrite side arms as a function of welding speed.
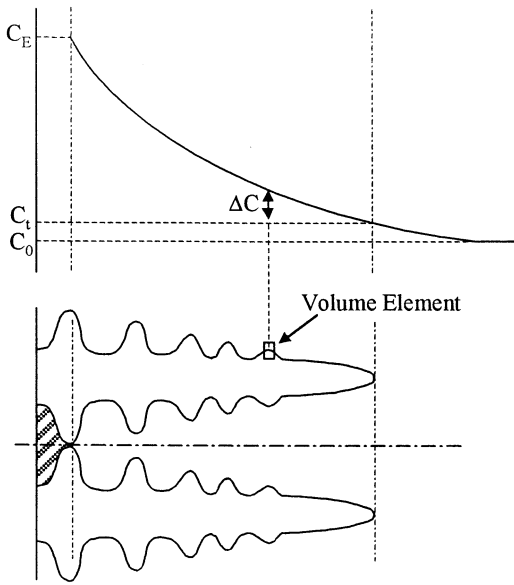
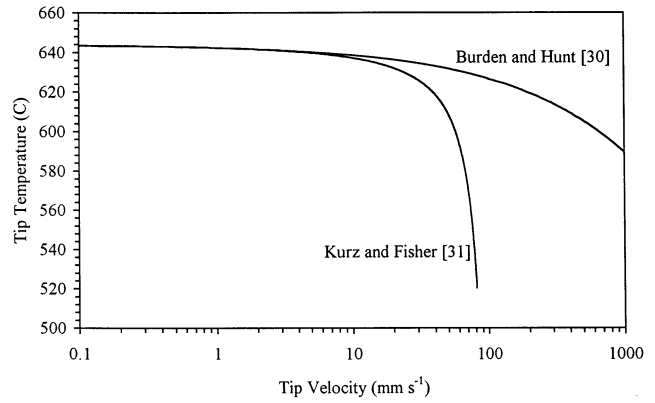Fig. 7. Schematic diagram illustrating a possible solute profile in the liquid during dendritic growth.

Fig. 8. Plot of primary tip velocity versus calculated primary tip temperature for a binary Al–4.46 wt% Cu alloy using the models of Burden and Hunt [30], and Kurz and Fisher [31].

Models have been developed to predict the primary dendrite tip undercooling which can, in turn, be related to the primary tip composition. According to Brody [28], the tip undercooling can be estimated from the following relationship.

$$\Delta T_{\text{tip}} = \Delta T_{\text{D}} + \Delta T_{\text{r}} + \Delta T_{\text{k}} \tag{7}$$

where ΔT_{D} is the diffusional undercooling, ΔT_{r} is the contribution of the undercooling due to curvature effects, and ΔT_{k} is the kinetic undercooling (the kinetic undercooling is the smallest contribution to undercooling in an alloy, and according to Chalmers [29], can be neglected in this analysis). This approach has been used by Burden and Hunt [30] to derive an expression for tip undercooling by assuming the tip grows at the minimum undercooling:

$$\Delta T = \frac{GD_{\text{L}}}{V} + \sqrt[3]{2}\frac{\sqrt{-mV(1-k)C_0\theta}}{\sqrt{D_{\text{L}}}} \tag{8}$$

where V is the tip velocity, D_{L} is the solute diffusivity in the liquid, m is the liquidus slope, and θ is the curvature undercooling coefficient.

More recently, Kurz and Fisher [31] have pointed out that the minimum undercooling criteria underestimates the change in tip temperature, and have instead, used the criteria that the tip radius is equal to the wavelength of instability of the interface. In both approaches, the tip temperature is dominated by the growth velocity, rather than the thermal gradient, when the growth velocities are higher than 10^{-3} cm s^{-1} and therefore in the range of interest to welding. Both models show that the tip undercooling starts to rapidly increase at high velocities (~1 cm s^{-1}) although the Kurz and Fisher

model predicts that this will occur at a greater rate (Fig. 8). Using the Kurz and Fisher model, the variation in tip undercooling has been translated to a core composition for the growth of primary dendrites in a binary Al–4.46 wt% Cu alloy, and the data is shown in Fig. 9 together with the measured values for the secondary arms. By assuming that the primary tip velocity is the same as the welding speed, the model of Kurz and Fisher demonstrates that as the welding speed is increased, so the primary tip concentration also increases, i.e. in agreement with the trends of this work. As might be expected from Fig. 7, the predicted composition values for the primary tip (kC_{t}) are somewhat less than the measured values of $k(\Delta C + C_{\text{t}})$, for the secondary arm core compositions. However the secondary arm core composition does increase with increasing welding speed in line with the predicted primary tip behaviour.
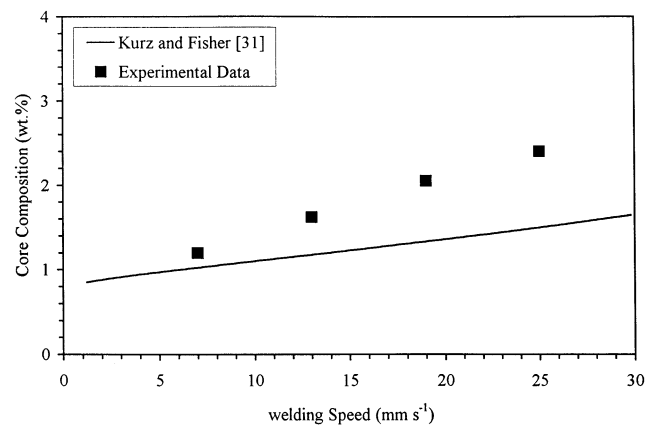

Fig. 9. Comparison between the predicted core compositions of the primary dendrite (C_{t}) taken from the model of Kurz and Fisher [31] and the measured core concentrations from the dendrite side arms as a function of welding speed (it is assumed that the primary tip grows at the same velocity as the welding speed).

6. Conclusions

A detailed understanding of the effect of the processing conditions is required to produce a good weld microstructure for the autogenous TIG welding of the commercial aluminium alloy AA2024. At high welding speeds and low power densities, it is possible to promote the formation of an equiaxed-dendritic microstructure in the centre of autogenous welds. This is due to the development of an undercooled liquid ahead of the moving solid–liquid interface, which provides the correct thermal conditions for the nucleation and growth of new grains. The most likely origin for the nucleants is expected to be from a combination of dendrite arm detachment and TiB_2 particles that survive in the melt.

The finest microstructure was observed at the centre of the weld and is attributed to the higher cooling rates at the weld centre compared to those at the fusion boundary. As the welding speed was increased, the cooling rate at the centre of the weld also increased producing a reduction in the scale of the dendrite secondary arm spacing.

Both the dendrite side arm spacing and the microsegregation behaviour have been investigated using quantitative EDX analysis. The microsegregation behaviour of the dendrite side arms has been shown to follow a Scheil type behaviour in which there appears to be negligible back diffusion in the solid. However, the core concentration within a dendrite side arm substantially changes with the welding speeds used in TIG welding. This behaviour can be explained in terms of the formation of significant undercoolings ahead of the primary dendrite tip which enriches the liquid surrounding the dendrite side arms.

Acknowledgements

References

[1] J.R. Davis (Ed.), ASM Speciality Handbook: Aluminium and Aluminium Alloys, ASM International, Metals Park, OH, 1993, p. 376.

[2] R. Onjukka, Weld. J. 75 (1996) 29.

[3] S. Kou, Weld. Res. Council Bull. 320 (1986) 1.

[4] R.V. Ilyushenko, Aluminium 69 (1993) 364.

[5] V.V. Grinin, A.V. Petrov, V.V. Ovchinnikov, Weld. Prod. 33 (1986) 19.

[6] I.N. Fridlyander, in: T.H. Sanders, Jr., E.A. Starke, Jr. (Eds.), Proceeding of the 5th International Conference on Al–Li Alloys, Williamsburg, Virginia, 1989, MCEP, Birmingham, 1989, p. 1359.

[7] D.E. Schillinger, I.G. Betz, F.W. Hussey, H. Markus, Welding J. 42 (1963) 269S.

[8] W.I. Pumphrey, J.V. Lyons, J. Inst. Metals 74 (1948) 439.

[9] T. Ganaha, B.P. Pearce, H.W. Kerr, Metall. Trans. A 11 (1980) 1351.

[10] S. Kou, Y. Le, Weld. J. 65 (1986) 305S.

[11] Y. Arata, F. matsuda, A. Matsui, Trans. Jpn. Weld. Res. Inst. 3 (1974) 89.

[12] M. Rappaz, C.A. Gandin, J.L. Desbiolles, P. Thevoz, Metall. Trans. A 27 (1996) 695.

[13] J.A. Brookes, M.J. Baskes, in: S.A. David (Ed.), Advances in Welding Science and Technology, ASM International, Metals Park, OH, 1987, p. 93.

[14] S.A. David, J.M. Vitek, Int. Mater. Rev. 34 (1989) 213.

[15] H. Jones, Monograph No. 8, Institute of Metallurgists, London, 1982.

[16] E. Scheil, Z. Metallkd. 34 (1942) 70.

[17] H.D. Brody, M.C. Flemings, Trans. AIME 236 (1966) 615.

[18] Ø. Grong, in: H.K.D.H. Bhadeshia (Ed.), Metallurgical Modelling of Welding, Institute of Materials, London, 1994.

[19] J.D. Hunt, Mater. Sci. Eng. 65 (1984) 75.

[20] D.G. McCartney, Int. Mater. Rev. 34 (1989) 247.

[21] R. Trivedi, W. Kurz, Int. Mater. Rev. 39 (1994) 49.

[22] D. Rosenthal, Weld. J. 20 (1941) 220s.

[23] D. Rosenthal, Trans. ASME 68 (1946) 849.

[24] A.F. Norman, K.E. Jakielski, G. Scott, P.B. Prangnell, in: J. Beech, H. Jones (Eds.), Proceedings of the 4th International Conference on Solidification Processing, University of Sheffield, December 1997, p. 670.

[25] S.L. Chen, Y. Zuo, H. Liang, Y.A. Chang, Metall. Trans. A 28 (1997) 435.

[26] N. Saunders, Mater. Sci. Forum 217-222 (1996) 667.

[27] A.F. Norman, P.B. Prangnell, in: T. Sato, S. Kumai, T. Kobayashi, Y. Murakami (Eds.), Proceedings of the 6th International Conference on Aluminium Alloys (ICAA-6), Japan Institute of Light Metals, Japan, 1998, p. 1435.

[28] H.D. Brody, in: S.A. David (Ed), Advances in Welding Science and Technology, ASM International, Metals Park, OH, 1987, p. 83.

[29] B.A. Chalmers, Principles of Solidification, Wiley, New York, 1964.

[30] M.H. Burden, J.D. Hunt, J. Crystal Growth 22 (1974) 109.

[31] W. Kurz, D.J. Fisher, Acta Metall. 29 (1981) 11.